2011

Reduced auger recombination in mid-infrared semiconductor lasers

Robert Bedford

Gregory Edward Triplett
Virginia Commonwealth University, getriplett@vcu.edu

David H. Tomich

See next page for additional authors

Authors

Robert Bedford, Gregory Edward Triplett, David H. Tomich, Stephan W. Koch, Jerome Moloney, and Jorg Hader

Reduced auger recombination in mid-infrared semiconductor lasers

Robert G. Bedford, Gregory Triplett, David H. Tomich, Stephan W. Koch, Jerome Moloney, and Jörg Hader

---

Articles you may be interested in

Band parameters for III–V compound semiconductors and their alloys
Journal of Applied Physics **89**, 5815 (2001); 10.1063/1.1368156

Auger coefficients in type-II $InAs/Ga_{1-x}In_xSb$ quantum wells
Applied Physics Letters **73**, 2857 (1998); 10.1063/1.122609

Room-temperature vertical-cavity surface-emitting lasers at 4 µm with GaSb-based type-II quantum wells
Applied Physics Letters **110**, 071104 (2017); 10.1063/1.4975813

Extended short-wavelength infrared nBn photodetectors based on type-II InAs/AlSb/GaSb superlattices with an AlAsSb/GaSb superlattice barrier
Applied Physics Letters **110**, 101104 (2017); 10.1063/1.4978378

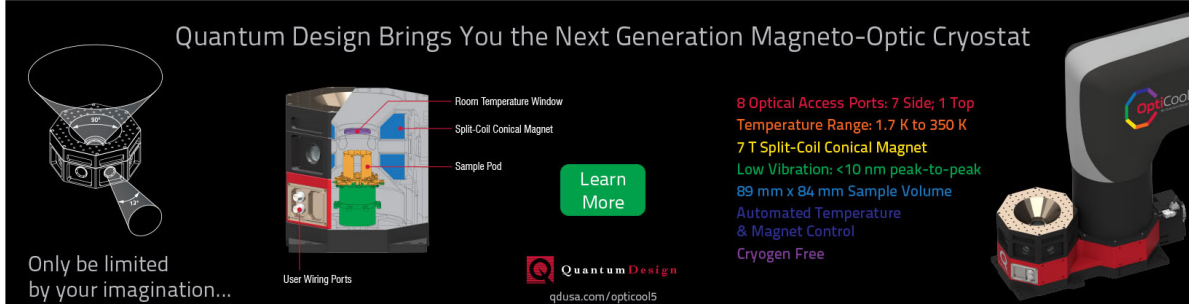GaSbBi/GaSb quantum well laser diodes
Applied Physics Letters **110**, 222106 (2017); 10.1063/1.4984799

GaSb superluminescent diodes with broadband emission at 2.55 µm
Applied Physics Letters **112**, 051106 (2018); 10.1063/1.5015974

Reduced auger recombination in mid-infrared semiconductor lasers

Robert G. Bedford,[1,a)] Gregory Triplett,[2] David H. Tomich,[1] Stephan W. Koch,[3] Jerome Moloney,[4] and Jörg Hader[4]

[1]*Air Force Research Laboratory, Sensors Directorate Wright-Patterson Air Force Base, Ohio 45433, USA*
[2]*University of Missouri, Department of Electrical and Computer Engineering Columbia, Missouri 65211, USA*
[3]*Phillips Universität Marburg, Department of Physics and Material Sciences Center Marburg, Germany 35032*
[4]*Nonlinear Control Strategies, Inc., Tucson, Arizona 85705, USA*

A quantum-design approach to reduce the Auger losses in $\lambda = 2$ μm InGaSb type-I quantum well edge-emitting lasers is reported. Experimentally realized structures show a $\sim 3 \times$ reduction in the threshold, which results in $4.6 \times$ lower Auger current loss at room temperature. This is equivalent to a carrier lifetime improvement of $5.7 \times$ and represents about a 19-fold reduction in the equivalent "Auger coefficient." © *2011 American Institute of Physics*. [doi:10.1063/1.3646552]

I. INTRODUCTION

Lasers emitting in the infrared regime of the electromagnetic spectrum have many applications in the sensing community, including remote chemical sensing of numerous organic compounds such as methane.[1] Furthermore, these lasers are ideal sources for low-altitude laser radar[2] and, if sufficiently bright, infrared countermeasures. Although there are several potentially successful approaches to developing semiconductor sources in different parts of the infrared regime, as one approaches the 2–4 μm band, challenges exist that must be overcome for successful system adoption.

Within the last 15 years, quantum cascade lasers (QCLs) have proven to be a very capable semiconductor laser platform, owing to the ability to rely on an engineered bandgap approach utilizing intersubband transitions, making them very attractive for low energy lasers. However, these lasers are limited by band offset in the conduction band,[3,4] and the desire for higher energy sources is progressing toward more exotic material system.[5,6] Equally as promising are type-II quantum well lasers which rely on electron- and hole-confinement in adjacent layers, which can reduce the Auger coefficient by an order of magnitude when compared to commensurate type-I quantum wells.[7,8] As these layers are made sufficiently thin, their electronic wavefunctions have significant overlap, and are well suited for wavelengths above ~ 2.8 μm, although are somewhat restricted at the longer wavelengths, compared to QCLs due to band filling.[9] In the short-wave and mid-wave infrared wavelengths, their low T_0 necessitates low temperatures to achieve appreciable powers, even with five or more quantum wells.[7]

Type-I quantum well lasers can also address the 2–4 μm wavelength band. Although immature relative to III-P and III-As systems, GaSb provides a reasonably flexible platform for the (AlGaIn)(AsSb) material system, and allows for various bandgaps, refractive index-, and strain-profiles within the active region. Ternary InGaAs quantum wells[10] are suita-

ble for $\lambda \lesssim 2.1$ μm, but are generally restricted to low compositions of indium and thin layers to avoid excessive strain. At longer wavelengths, it becomes necessary to use the InGaAsSb quaternary quantum well to control strain and achieve higher indium concentration.[11] Utilizing a "quinternary" barrier material of InAlGaAsSb, researchers have demonstrated room temperature cw operation well over 3 μm.[12,13] Performance of this material system suffers at longer wavelengths, due primarily to increased Auger recombination.

We choose to approach the problem by addressing the Auger recombination mechanisms directly and demonstrate this capability in the region of $\lambda = 2$ μm. In Sec. II, we address the principles of Auger recombination mitigation, and outline our approach. In Sec. III, we describe the growth and fabrication of broad area lasers used to measure the Auger carrier losses, followed by our results and discussion in Sec. IV. Some concluding remarks are given in Sec. V.

II. AUGER ENGINEERING PRINCIPLES

Type-I quantum well lasers are attractive at wavelengths below about 2 μm, but at longer wavelengths, they tend to suffer from increased Auger losses, as the photon energies become resonant with higher subbands. Empirically, the Auger loss current is nominally proportional to N_{th}^3, where N_{th} is the threshold carrier density. A reduction in N_{th} has been the most common approach to achieving efficient lasers. Even then, it has been shown that the proportionality constant (known as the "Auger coefficient," and typically denoted as C) dramatically increases above 2 μm (Ref. 14).

The carrier density dependence of the Auger coefficient itself is not commonly considered, which results in less than optimized, and sometimes incorrectly designed structures. In our calculations, we avoid this empirical relation, rather calculating the Auger processes using quantum many-body theory. This approach is used to determine a carrier-dependent lifetime (τ) which we use to evaluate quantum well design. The typical approximations used for Auger scattering equations which utilize simplified Coulomb coupling

a)Author to whom correspondence should be addressed. Electronic mail: robert.bedford@wpafb.af.mil.

matrix elements predict values for Auger recombination which deviate from actual values by an order of magnitude.

For the purposes here, we use semiconductor Bloch equations and quantum Boltzmann scattering to determine dephasing of P, the macroscopic optical polarization, calculated from the microscopic polarizability as well as the absorption/gain line shape.[15] Spontaneous emission is determined using semiconductor luminescence equations with higher order Coulomb correlation source terms. These rigors avoid issues with line shape errors as well as spectral position inaccuracies with respect to carrier density and temperature.

Critical to narrow bandgap structures, Auger recombination calculations utilize scattering equations in the second Born-Markov approximation with fully resolved k-, spin-, and subband-summations as well as z-integrals. This technique is more thoroughly discussed in Ref. 16. The gain model requires only inputs defining structural layout (layer widths, compositions) and basic bulk band structure parameters (e.g., Luttinger parameters, band gaps, and band offset[17]). When comparing to experiments, the only unknown parameters are therefore inhomogeneous broadening, shockley-read-hall (SRH) recombination, pump efficiency and internal modal optical loss. These parameters may be measured independently, and will vary depending on factors such as interface quality and compositional control.

We then use the results of our microscopic calculations as input for a simple set of above—threshold rate equations:

$$\frac{dN}{dt} = \eta i \frac{J}{M} - \left(\frac{1}{\tau_a} + \frac{1}{\tau_b} + \frac{1}{\tau_c}\right)N - v_g g N_p, \qquad (1)$$

$$\frac{dN_p}{dt} = -\frac{N_p}{\tau_p} + v_g(\Gamma g - \alpha)N_p. \qquad (2)$$

Here, N is the 2D carrier density, η_i is dominated by the optical absorption, and is analogous to internal quantum efficiency. The carrier excitation by the pump is denoted as J ($J \equiv \Phi/\hbar\omega_p$), and where J/M is the mean carrier excitation per well. For a small number of wells ($M \lesssim 4$), carriers are distributed relatively evenly throughout multiple wells when the stimulated lifetime does not overwhelm the inter-well transport.[18] The SRH, spontaneous, and Auger lifetimes are given by $\tau_{a,b,c}$, respectively. The quantum well gain is g, N_p is the 2D photon density, τ_p is the geometric photon lifetime, Γ is the 3D mode overlap with all of the quantum wells, and α is the waveguide loss. In arriving at Eqs. (1) and (2), we

ignore carrier exchange between the barriers and wells due to the low barrier carrier density, accounting for these carriers as if they were generated directly in the well, although it should be noted this exchange is included within the gain calculation. Including them would provide a third equation describing the rate of barrier-generated carriers. Test calculations show that the influence of these barrier states on the gain remains a small ($\sim$1%) correction to Eqs. (1) and (2) which we do not include in our present studies. We also ignore the contribution of spontaneous emission to photon density. Our detection scheme does not have sufficient sensitivity to discern this contribution near and below threshold, and spontaneous emission is negligible above threshold.

There are many types of Auger recombination that can occur in the infrared emitting laser structures. In this wavelength regime, Auger losses are dominated by processes in which an electron and hole recombine and the excess energy is used to excite another electron high into a conduction subband (CHCC process),[19] and depend strongly on details of the band structure. Generally, when varying the barrier potential, ΔE_c, the dominant factor is the excess photon energy (E_g) with respect to the barrier level. Commonly, the approach is to design for a large ΔE_c, reducing carrier density. The reduced carrier density is intended to improve the Auger lifetime through the empirical relation:

$$C \equiv \left(\tau_c N_{th}^2\right)^{-1}, \qquad (3)$$

where C is known as the Auger coefficient. However, for a given wavelength, the Auger lifetime lifetime can vary dramatically, primarily depending on the E_g relation to ΔE_c.

In Fig. 1(a), we present results where we compute the lifetimes at 300 K, holding the gain constant while adjusting carrier density to compensate varied differential gains. The separate contributions to the carrier lifetime (spontaneous and Auger lifetimes) are plotted as a function of barrier height in empty- and filled-symbols. Here, we use a threshold of 600 cm^{-1}, which is a reasonable approximation for our devices. Assuming a SRH lifetime of 4.5 ns (also determined through fitting to experimental data, as shown in Section IV), the total carrier lifetimes are also shown (solid black lines). Theses lifetimes are calculated for various threshold gains between 200 cm^{-1}−1000 cm^{-1}, with the data corresponding to 600 cm^{-1} specifically identified through the gray fill beneath it. Because the Auger recombination is sensitive to subband positioning, and these structures are dominated by CHCC processes, the conduction subband positions are plotted relative to the lowest electronic subband in Fig. 1(b).

In the infrared wavelength regime, E_g is typically much larger than ΔE_c in the laser materials. For Auger recombination in this region, the final electron is excited into states that are delocalized in the barrier, and are reasonably approximated by bulk-states. A transition from a confined subband to this delocalized band requires a large transfer of momentum.[20] Because the Coulomb matrix elements that mediate the Auger transitions strongly decrease with a change in momentum, the Auger lifetime increases with increasing excess energy above the barrier level.

TABLE I. Tabulated experimental results presented in this paper for high-barrier (HB), medium- barrier (MB) and low-barrier (LB) structures. We include the calculated conduction-band offsets, measured J_{th}/M calculated contribution from Auger currents (J_a/M), Auger lifetimes and calculated Auger coefficients (relative to the HB structure), and measured T_0 values

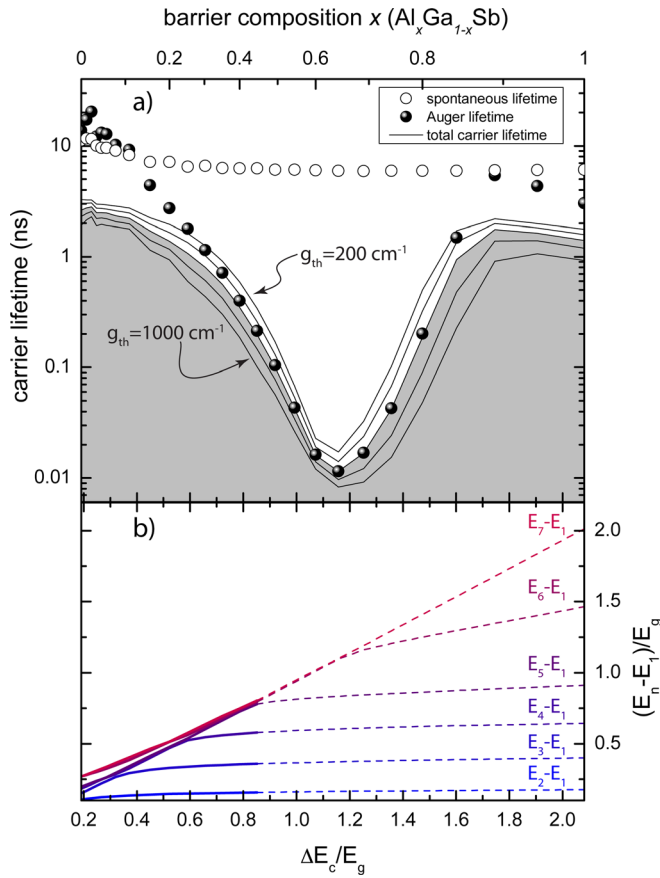|	$\Delta E_c/E_g$	J_{th}/M (A/cm^2)	J_c/M (A/cm^2)	τ_c/τ_c^{HB}	C/C^{HB}	T_0 (K)
HB	0.76	480	377	1.00	1.00	69
MB	0.62	283	179	3.05	0.16	67
LB	0.30	255	124	5.67	0.05	57

FIG. 1. (Color online) (a) Contributions to room temperature carrier lifetime as a function of ΔE_c. Spontaneous and Auger lifetimes are given for $g_{th} = 600$ cm^{-1}. Total carrier lifetimes (including an SRH lifetime of 4.5 ns) are given for g_{th} of 200, 400, 600, 800, and 1000 cm^{-1}. The total carrier lifetime associated with the spontaneous and Auger lifetimes plotted is emphasized with a shade underneath. (b) transition energies between the lowest conduction band state and excited states. The drop of Auger lifetime in the region that $\Delta E_c/E_g \simeq 1$ indicates the increased availability of states available for Auger transitions.

At higher barriers ($\Delta E_c/E_g \gtrsim 0.5$), Auger recombination dominates the carrier lifetime as the $E_g \simeq \Delta E_c$. This is due, in part to carrier excitations to more localized wavefunctions resulting in reduced momentum transfer. Within this region, coupling is very dependent on band-structure. There is a precipitous dip around $\Delta E_c \simeq E_g$, where transitions require less momentum exchange. This dip is not at exactly at $\Delta E_c/E_g = 1$ because the lowest quantized conduction band state is slightly above the well band-edge. Moreover, the $E_6 - E_1$ and $E_7 - E_1$ are close to E_g, which promotes resonant transitions; the transition probability between these excited electronic states increases dramatically, causing the Auger lifetime to drop to around 10 ps. This calculation provides insight into why lowering N_{th} is not always an effective approach to control of Auger processes. An increased differential gain (through larger ΔE_c) is often coupled with an elevated Auger coefficient, diminishing the returns of the lower operating carrier density.

At barrier heights where $\Delta E_c/E_g > 1$, the final excited state is confined within the quantum well and transfer from the lowest-subband requires no additional in-plane momentum. This region can also have low Auger recombination
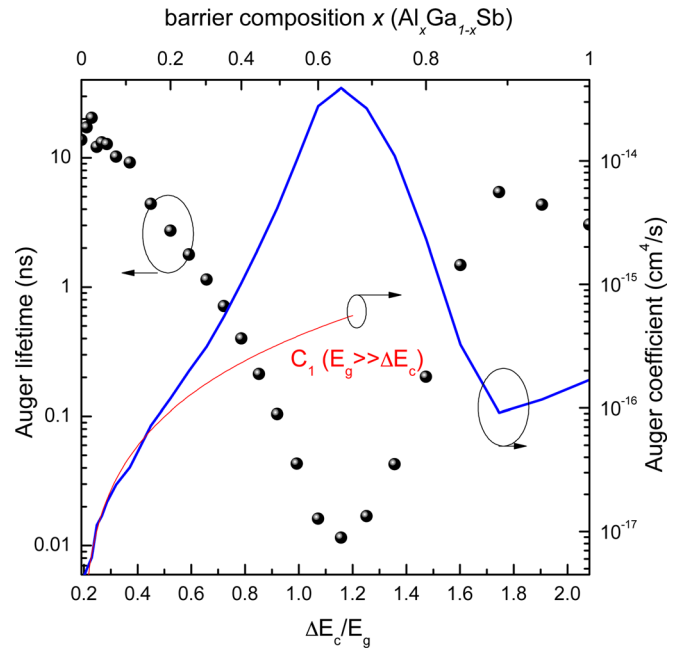

FIG. 2. (Color online) Comparison of calculated Auger lifetime vs Auger coefficient, where the latter (C) is taken to be equivalent to $(\tau_c N_{th}^2)^{-1}$. C_1 for the CHCC process as given in Ref. 20. Varying the structure while keeping the bandgap essentially constant, the Auger coefficient can change by two orders of magnitude.

provided there is no resonant excited subband. However, the Auger lifetime becomes short as the excited subband is about E_g above the lowest electronic subband ($E_n - E_1 \approx E_g$). Figure 1 shows evidence of this shortened Auger lifetime as E_g moves closer to the $E_5 - E_1$ transition, in the region where $\Delta E_c/E_g \sim 2$.

In Fig. 2, we compare the microscopically computed Auger lifetime to the phenomenological relation in Eq. (3). This relation ($\tau_c \propto C^{-1}$) is the dominant factor in the calculations shown in Fig. 2, because at larger values of ΔE_c, N_{th} is approximately constant. At very low values of ΔE_c, N_{th} increases dramatically due to the poor carrier confinement, and this relation ($\tau \propto C^{-1}$) deviates significantly. We also show the approximation from Ref. 20 for the CHCC coefficient for the case where $E_g \gg \Delta E_c$.

III. SAMPLES, GROWTH AND FABRICATION

In order to test the theoretical predictions, we experimentally analyze three different gain-guided laser structures all operating at nominally 2 μm which show a "standard" type - I quantum well and two structures having similar wells but modified barriers to adjust the subband offset. The reference system utilizes an In$_{0.28}$Ga$_{0.72}$Sb quantum well surrounded by Al$_{0.3}$Ga$_{0.7}$Sb barriers, resulting in an $\Delta E_c \sim 0.46$ eV, where the emitted photon energy is about 0.61 eV. This high barrier structure, herein referred to as "HB," has strong electron and hole confinement with three fully confined electron and hole levels. This strong confinement results in a large differential gain thus allowing for low N_{th} lasers.[21] However, as mentioned earlier, a low carrier density is not necessarily the best approach if one want to optimize the Auger losses simultaneously.

To test this, we design two additional structures with reduced barriers. In order to compare structures of similar E_g, the indium composition in the quantum well is decreased to 0.2 and the well is widened to 12 nm, allowing us to achieve lower values of ΔE_c. These two additional structures have barrier materials composed of $Al_{0.25}Ga_{0.75}Sb$ and $Al_{0.05}Ga_{0.95}Sb$, and are given the identifiers "MB" and "LB," respectively. The MB structure has a calculated ΔE_c of 0.38 eV while the ΔE_c calculated for the LB structure is only 0.18 eV. The ratio $\Delta E_c/E_g$ is 0.76, 0.62, and 0.30 for HB, MB, and LB, respectively. Only the LB structure is well approximated by the coupling from the discrete to the continuous spectrum in the conduction band.[20]

We produce strained $In_xGa_{1-x}Sb/Al_yGa_{1-y}Sb$ quantum well structures using solid-source molecular beam epitaxy (MBE) system. Semi-insulating GaSb substrates are mounted in indium-free molybdenum blocks with diffuser plates (located between the substrate and the substrate heater) to achieve improved temperature uniformity across the wafer. During substrate outgassing, deoxidation temperatures are monitored using a 10 keV reflection high - energy electron diffraction (RHEED) system and are confirmed by a "1 × 3" reconstruction pattern. The growth temperatures are relative to the GaSb deoxidation temperature and also referenced by the "1 × 5" phase transition while under antimony over-pressure. Prior to laser growth and to ensure precise alloy composition and thickness for each laser design presented, deposition rates are varied, measured *in situ* by RHEED, and confirmed *post-growth* using high-resolution x-ray diffraction (HR-XRD). Samples are also analyzed by atomic force microscopy (AFM), which demonstrates that these structures were indeed produced via step flow growth. Figure 3 illustrates a $\Theta - 2\Theta$ HR-XRD scan (with accompanying simulation data) and an AFM image of AlSb/GaSb superlattices produced prior to laser growth.

$In_xGa_{1-x}Sb$ structures are also produced to calibrate indium composition in the quantum well and to ensure 2 μm emission, which is confirmed with photoluminesence. For each laser design, the MBE process conditions (flux ratio, substrate temperature, and deposition rate) are selected to ensure quality and composition of each binary and ternary

layer. The shutter sequence and antimony valve-positioner are computer controlled, thus maintaining run-to-run consistency. Each quantum well/barrier combination is embedded in an AlGaSb waveguide that is adjusted to maintain a pump absorption of approximately 85%, and a transverse mode overlap of about 5%. In order to accomplish this, HB and MB structures have three repeats of the quantum wells, each separated by 100 nm to assure electronic isolation. To achieve the same overlap and absorption, while maintaining single transverse mode operation, the LB structure necessitates only two quantum wells.

As the gain-guided structures are defined by the optical pump, no lithographic steps are necessary. The bare wafers are thinned to nominally 80 μm using mechanical lapping and then cleaved into bars of various lengths (375 μm to 1500 μm). In this report, only 1500 μm length cavities are used.

IV. EXPERIMENT RESULTS AND DISCUSSION

Laser bars are mounted epitaxial-side up using thermal paste to a low-oxygen copper heat sink temperature controlled using a two-stage thermoelectric cooler, allowing various temperatures at, and around room temperature (from about 265 K to 325 K). We maintain a slow dry nitrogen purge to avoid condensation at temperatures below the dew-point. The lasers are pumped using a 980 nm semiconductor laser bar with a spot 125 μm wide and 3 mm long. Pulses are 2 μs long with a 1 kHz pulse repetition frequency, avoiding thermal loading.

A fraction of the optical power is collected using a fiber-coupled extended-range InGaAs detector. Both the pump laser and the device powers are time-gated to remove pulse transients. The pump power is measured directly using a fast InGaAs detector after determining the detector's linear response under CW conditions. While the detected device power remains uncalibrated, lasing threshold is the most important metric to evaluate carrier losses and therefore device powers remain in arbitrary units, although the noise floor of this detector is ∼0.01 on this arbitrary scale. Finally, we also record spectra at each temperature and pump level to confirm that the device is behaving as expected.

We measure the power characteristics of approximately 350 lasers spanning the three growth designs mentioned in Sec. II, and report these in Fig. 4. The mean data from each of the three structures are indicated by the data points, while the error bars signify standard deviation of the collected data.

Although the excitation is pulsed to avoid thermal loading, we ignore transients allowing us to set the left sides of Eqs. (1) and (2) to zero to find the steady state. In this case, we find the threshold condition of the laser:

$$\frac{\eta_i J_{th}}{M} = \frac{N_{th}}{\tau} \equiv \frac{N_{th}}{\tau_a} + \frac{N_{th}}{\tau_b} + \frac{N_{th}}{\tau_c}. \qquad (4)$$

Figure 4 shows the power characteristics of these lasers. The absorbed pump fluence per well is equivalent to $\eta_i J \hbar \omega_p / M$ in Eq. (1), and is, of course, the driving term of the laser. It is immediately evident that the HB structure has the highest
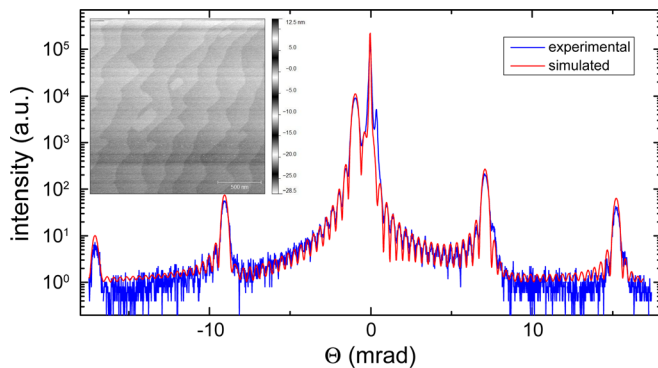

FIG. 3. (Color online) Example of HR-XRD $\Theta - 2\Theta$ rocking curves of AlSb/GaSb superlattices along with calculated diffraction pattern, representing faithful reproduction material composition and layer thickness. Inset is as example surface profile measurement by AFM.
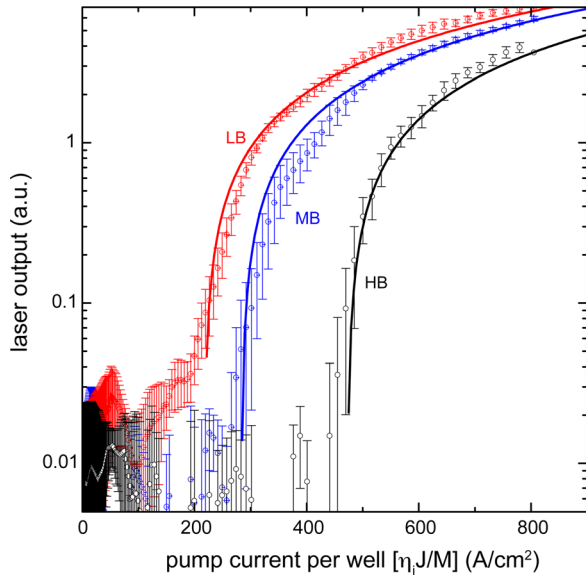
FIG. 4. (Color online) Laser power characteristics given for the three designs outlined in Sec. II, as a function of equivalent pump current density.
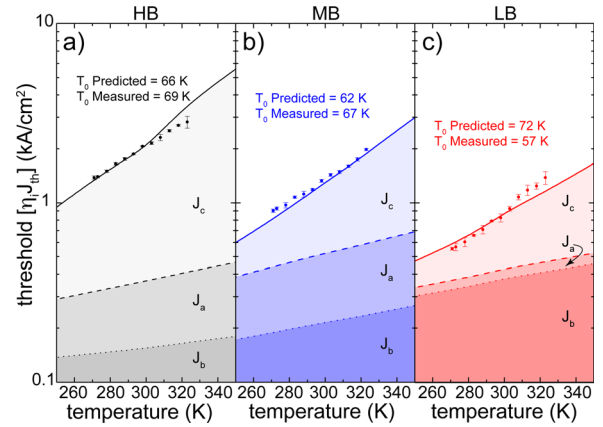

FIG. 5. (Color online) Threshold (in equivalent current) and T_0 and contributions from the three carrier loss contributors $J_{a,b,c}$ for (a) the HB structure, (b) the MB structure, and (c) the LB structure.

threshold per well, a result that is not unpredictable due to the large Auger recombination as discussed in Sec. II and calculated in Fig. 1.

From Fig. 4, we see that the thresholds per well is 480, 283, and 255 Acm^{-2}/well, which correspond to equivalent pump fluences of 606, 358 and 322 Wcm^{-2}/well for the HB, MB, and LB structures, respectively. Experimental results compare favorably to theory in the MB and HB structures for an internal absorption $\alpha_i = 10$ cm^{-1} and a SRH lifetime $\tau_a = 4.5$ ns. In contrast, the LB structure had a larger internal loss of $\langle \alpha_i \rangle = 20$ cm^{-1}, but the SRH lifetime was found to be larger as well (20 ns), offsetting some of this additional loss. This is not altogether surprising because the LB structure, with only two wells, contains fewer interfaces within the high carrier density region, where SRH recombination typically presents itself. However, the transverse mode profile contains longer tails and therefore could incur higher losses due to optical scattering.

From these parameters, we determine the threshold carrier densities to be 1.15×10^{12} cm^{-2}, 1.67×10^{12} cm^{-2}, and 2.12×10^{12} cm^{-2} for the HB, MB, and LB structures, respectively. We use this to compute the carrier lifetimes for the MB and LB structures as $2.46\times$ and $6.56\times$ that of the HB "standard" structure, representing a significant ($>6\times$) improvement of the carrier lifetime, resulting in a significantly lower threshold density. Within the parameter constraints of these structures, the total carrier lifetime is measured to be as long as $\sim$2 ns, limited by SRH recombination. However, according to Fig. 1, improving interface quality should bring the carrier lifetime up to almost 9 ns (Table I).

A more definitive test of the model and the device improvement is the temperature dependence of the threshold, and therefore loss mechanisms. This dependence is commonly denoted as T_0 and empirically behaves as an exponential growth.[19] Although this relation is not completely accurate,[16] it is often a suitable fit for a wide variety of temperatures.

Figure 5 shows the temperature-dependence of the HB [Fig. 5(a)], MB [Fig. 5(b)], and LB [Fig. 5(c)] structures. These curves, while including the η_i term, are not normalized by the number of wells as in Fig. 4. We also show in Fig. 5 the calculated contributing terms to the total threshold fluence. In each case, the relative contribution of the SRH, spontaneous, and Auger are denoted by $J_{a,b,c}$, respectively, and are computed as a function of temperature. The same terms for $\langle \alpha_i \rangle$ and τ_a are used for this graph as those used to compare in Fig. 4.

We can see in each of these examples, the measured T_0 is closely predicted by the model. In the best case, these deviated by 3 K for the HB structure. We expect the kink at about 300 K should have been more evident. This kink is due to increased Coulomb matrix elements as E_g drops at higher temperatures approaching ΔE_c, where less momentum is required for the transition. In the worst case, this deviation was as high as 15 K for the LB structure, although this effect could be attributed to carrier transport effects such as thermionic emission, which are not considered in our calculations.

For all of our lasers, we compare the fraction of Auger recombination to that of the standard HB structure. Despite the increased threshold carrier density, we indeed find that J_c is reduced from 1.13 kA/cm^2 to 0.25 kA/cm^2, a fourfold decrease in carrier losses due to Auger recombination from the HB structure to the LB structure. Accounting for threshold carrier density disparity, this reflects a $5.7\times$ increase in Auger recombination lifetime, reflecting a significant improvement of the Auger losses.

The phenomenological Auger coefficient (C), related to τ_c by Eq. (3), is often used to evaluate device performance. Although this criterion is not as useful to benchmark as the direct lifetime, we can calculate the value of C relative to the HB structure for reference; this value is found to be $6.4\times$ lower for the MB structure, and a significant $19.2\times$ lower for the LB structure. We show then that C, most often considered constant for a given bandgap, to be easily varied by $20\times$, and we can widen this more dramatically with stronger electron confinement (as high as $\sim$0.55 eV with barriers composed of Al$_{0.45}$Ga$_{0.55}$Sb), although this would not further improve the device, but

rather make the lower performing devices less suitable. If similar improvements are made at longer wavelength type-I structures, performance could be comparable to type-II lasers.[8]

V. CONCLUSIONS

We have shown that we can quantum design the Auger recombination through detailed band structure engineering. We experimentally realize three different laser structures with various barrier heights and analyzed the room temperature power performance and the temperature-dependent threshold variation. We obtain an increase in the carrier lifetime of $> 6\times$. Our detailed theoretical analysis shows that most of this improvement is due to the improved Auger lifetime, with a lifetime as long as $\sim 5.7 \times$ that of the standard structure.

ACKNOWLEDGMENTS

[1]R. W. Russell, G. S. Rossano, M. A. Chatelain, D. K. Lynch, T. K. Tessensohn, E. Abendroth, D. Kim, and P. Jenniskens, Earth Moon and Planets **82**, 439 (2000).

[2]F. E. Hanson, P. M. Poirier, E. J. Schimitschek, and M. A. Arbore, Proc. SPIE **4377**, 155 (2001).

[3]J. Faist, F. Capasso, D. L. Sivco, A. L. Hutchinson, S.-N. G. Chu, and A. Y. Cho, Appl. Phys. Lett. **72**, 680 (1998).

[4]M. Razeghi, A. Evans, S. Slivken, and J.-S. Yu, Proc. SPIE **5738**, 1 (2005).

[5]D. G. Revin, J. W. Cockburn, M. J. Steer, R. J. Airey, M. Hopkinson, A. B. Krysa, L. R. Wilson, and S. Menzel, Appl. Phys. Lett. **90**, 021108 (2007).

[6]M. Nobile, H. Detz, A. M. Andrews, P. Klang, W. Schrenk, and G. Strasser, Proc. SPIE **7616**, 76160M (2010).

[7]J. R. Lindle, C. S. Kim, M. Kim, W. W. Bewley, C. L. Canedy, I. Vurgaftman, and J. R. Meyer, Proc. SPIE **7230**, 72300R (2009).

[8]W. W. Bewley, J. R. Lindle, C. S. Kim, M. Kim, C. L. Canedy, I. Vurgaftman, and J. R. Meyer, Appl. Phys. Lett. **93**, 041118 (2008).

[9]A. P. Ongstad, R. Kaspi, G. C. Dente, M. L. Tilton, R. Barresi, and J. R. Chavez, Appl. Phys. Lett. **92**, 141106 (2008).

[10]A. Härkönen, M. Guina, O. Okhotnikov, K. Röβner, M. Hümmer, T. Lehnhardt, M. Müller, A. Forchel, and M. Fischer, Opt. Express **14**, 6479 (2006).

[11]L. Shterengas, G. Belenky, G. Kipshidze, and T. Hosoda, Appl. Phys. Lett. **92**, 171111 (2008).

[12]G. L. Belenky, J. G. Kim, L. Shterengas, A. Gourevitch, and R. U. Martinelli, Electron. Lett. **40**, 737 (2004).

[13]G. Belenky, L. Shterengas, D. Wang, G. Kipshidze, and L. Vorobjev, Semicond. Sci. Technol. **24**, 115013 (2009).

[14]J. R. Meyer, C. L. Felix, W. W. Bewley, I. Vurgaftman, E. H. Aifer, L. J. Olafsen, J. R. Lindle, C. A. Hoffman, M.-J. Yang, B. R. Bennett, B. V. Shanabrook, H. Lee, C.-H. Lin, S. S. Pei, and R. H. Miles, Appl. Phys. Lett. **73**, 2857 (1998).

[15]M. Lindberg and S. W. Koch, Phys. Rev. B **38**, 3342 (1988).

[16]J. Hader, J. Moloney, and S. Koch, IEEE J. Quantum Electron. **44**, 185 (2008).

[17]S. Adachi, J. Appl. Phys. **61**, 4869 (1987).

[18]N. Tessler and G. Eisenstein, Appl. Phys. Lett. **62**, 10 (1993).

[19]G. P. Agrawal and N. K. Dutta, *Semiconductor Lasers,* 2nd ed. (Kluwer Academic Publishers, Norwell, MA, 1993).

[20]A. S. Polkovnikov and G. G. Zegrya, Phys. Rev. B **58**, 4039 (1998).

[21]J.-M. Hopkins, N. Hempler, B. Rösener, N. Schulz, M. Rattunde, C. Manz, K. Köhler, J. Wagner, and D. Burns, Opt. Lett. **33**, 201 (2008).